

Tuning the growth mode of nanowires *via* the interaction among seeds, substrates and beam fluxes†

Cite this: *Nanoscale*, 2014, 6, 8392Valentina Zannier,^{ab} Vincenzo Grillo,^{cd} Faustino Martelli,^e Jasper Rikkert Plaisier,^f Andrea Lausi^f and Silvia Rubini^{*a}

The growth mechanism of semiconductor nanowires is still an argument of high interest, and it is becoming clearer, investigation after investigation, that simple pictures fail to describe the complex behaviors observed under different growth conditions. We report here on the growth of semiconductor nanowires, maintaining control over the chemical composition and the physical state of the metallic seeds, and tuning the growth mechanism by varying the growth conditions. We focused on Au-assisted ZnSe nanowires grown by molecular beam epitaxy on GaAs(111)B substrates. We show that at sufficiently high temperatures, the Au seed is strongly affected by the interaction with the substrate and that nanowire growth can occur through two different mechanisms, which have a strong impact on the nanowire's morphology and crystal quality. In particular, ZnSe NWs may exhibit either a uniformly oriented, straight morphology when the nanoparticle seed is liquid, or a kinked, worm-like shape when the nanoparticle seed is switched to a solid phase. This switch, which tunes the nanowire growth mechanism, is achieved by controlling the Zn-to-Se beam pressure ratio at the Au-seed surface. Our results allow a deeper understanding of particle-assisted nanowire growth, and an accurate control of nanowire morphology *via* the control of the growth mechanism.

Received 4th March 2014

Accepted 24th April 2014

DOI: 10.1039/c4nr01183j

www.rsc.org/nanoscale

Introduction

Semiconductor nanowires (NWs) are attracting increasing interest due to their novel properties, which make them promising building blocks for electronic and optoelectronic devices.^{1–3} The full potential of these nanostructures, however, will only be realized when a deep understanding and accurate control of the growth process is reached. The nanoparticle-assisted bottom-up growth from vapor phase by means of molecular beam epitaxy (MBE) offers the possibility to have precise control of the growth parameters, which is essential for the achievement of this purpose. In this approach, a metal nanoparticle (NP) seed acts as a collector of atoms from the molecular beams and drives the one-dimensional growth of the semiconductor material. Gold is the most common metal used

to assist vapor-phase nanowire growth,⁴ and the most widespread method to generate the nanoparticles is dewetting a thin metal film deposited on the substrate. This process results in the formation of particles with size, shape and chemical composition that strongly depend on the nature of the substrate, the interaction between the metal film and the substrate, and the temperature at which this process occurs.^{5,6} The morphology and physical state of the nanoparticles affect the nanowire growth mechanism, playing a crucial role in determining the properties of the nanowires.^{7–9} In addition to the thermal history and the chemical interaction between the metal film and substrate, the total vapor pressure and the ratio between the NW-precursor pressure can also affect the composition and physical state of the NPs during their growth, dynamically changing the growth mechanism and the resulting properties of the wires. Kodambaka *et al.*¹⁰ reported the chemical vapor growth of Ge NWs assisted by Au nanoparticles, showing that the NW growth can occur with either liquid or solid particles at the same temperature, and the seed state depends on the total pressure in the growth chamber. Hillerich *et al.*¹¹ reported on the epitaxial growth of InP NWs from Cu NPs by metal–organic vapor phase epitaxy, showing the effect of the P/In pressure ratio on the particle composition, NW growth rate and mechanism. Gamalski *et al.*^{12,13} showed real time transmission electron microscopy studies of the formation and the evolution of Au seed particles during Ge NW growth. They found

^aIOM-CNR Laboratorio TASC, S.S. 14, Km 163.5, I-34149 Trieste, Italy. E-mail: rubini@iom.cnr.it; Fax: +39 040226767; Tel: +39 0403756437

^bPhD School of Nanotechnology, Department of Physics, University of Trieste, Via Valerio 2, I-34127 Trieste, Italy

^cIMEM-CNR, Parco Area delle Scienze 37/A, I-43010 Parma, Italy

^dNANO-CNR, Via Campi 213/A, I-41125 Modena, Italy

^eIMM-CNR, Via del Fosso del Cavaliere 100, I-00133 Roma, Italy

^fSincrotrone Trieste S.C.p.A., Elettra Laboratory, S.S. 14, Km 163.5, I-34149 Trieste, Italy

† Electronic supplementary information (ESI) available. See DOI: 10.1039/c4nr01183j

metastable AuGe particles, whose formation involved changes in composition, and pointed out the importance of the seed-particle configuration for the subsequent NW growth mechanism. Indeed, those NPs can either recrystallize or remain liquid during NW growth at the same temperature, depending on the Ge supersaturation, which can be controlled through the precursor partial pressure.

Different growth modes, arising from seed configuration and dynamic changes during growth, are often reflected in different wire shapes and crystal qualities.^{14,15} This suggests that growth parameters can be modulated to create the desired structures. For instance, Caroff *et al.*¹⁶ reported the full control of the crystal structure of InAs NWs by varying the wire diameter and growth temperature. Tian *et al.*¹⁷ also reported the synthesis of a kinked nanowire superstructure obtained by an iterative modulation of the gaseous reactant supply. Therefore, studying the effects of sample preparation and growth conditions on the NW growth mechanism can provide the necessary tools to achieve the control and tunability of the nanostructure properties.

As for the specific material we have chosen for our investigation, ZnSe, a Au-assisted vapor–solid–solid (VSS) growth mechanism has been reported for temperatures as high as 510 °C on ZnSe¹⁸ or oxidized silicon^{19–21} substrates. Similarly, the VSS mechanism for thin ZnSe NWs grown on GaAs(111)B has been reported at 300 °C.²¹ On the other hand, it is known that some Ga interdiffusion can occur upon annealing Au films at higher temperatures on GaAs substrates, a feature that may affect both the seed composition and the physical state. Cai *et al.*²² reported the growth of ZnSe NWs on GaAs at 530 °C, suggesting that the seeds consist of liquid Au–Ga alloy nanoparticles. However, they did not obtain long and uniformly oriented ZnSe NWs, but rather NWs showing a strong diameter-dependent growth direction. The vapor–liquid–solid (VLS) mechanism has also been invoked for the growth of ZnSe NWs with seeds melting at temperatures lower than the growth temperature (T_g), like Ga²³ or Au–Sn²⁴ and Au–Si²⁵ intermetallic compounds.

To reach a deeper understanding of NW growth, we have performed a detailed investigation of the growth mechanism of Au-induced ZnSe nanowires on GaAs(111)B by molecular beam epitaxy at a fixed T_g of 450 °C. As it will be shown in the following, this temperature is indeed sufficiently high to allow interaction of the Au film with the GaAs substrate, but also sufficiently low to allow effective growth of ZnSe NWs by MBE.²⁶ With the help of *in situ* and *ex situ* electronic and structural measurements, we show that due to the interplay between the substrate, metal, and beam fluxes, both VLS and VSS growth mechanisms may take place at this temperature. The occurrence of either mechanism has an impact on the NW morphology and nanoparticle composition, and can be controlled by the growth protocol.

Results and discussion

As briefly mentioned above, the NWs in this work have been grown at 450 °C on GaAs(111)B substrates. The annealing at this

T of deoxidized GaAs(111)B substrates covered with 1 nm Au results in the formation of nanoparticles with a size distribution between 15 and 65 nm, and a mean diameter of 30 nm. The subsequent ZnSe deposition at the same temperature leads to the growth of ZnSe NWs with the same density and diameter distribution and an almost uniform diameter over the whole length. However, the morphology of the NWs is strongly affected by the Zn/Se pressure ratio. Fig. 1 shows SEM images of ZnSe NWs obtained after 10 minutes deposition using a Zn/Se beam pressure ratio (BPR) of 0.4 (a) and 4 (b), respectively.

Under Se-rich conditions (BPR = 0.4), disordered and kinked nanowires grow, with a “worm-like” shape and without any preferential growth direction. Vertically oriented and straight ZnSe nanowires are obtained when the Zn/Se pressure ratio is increased (BPR = 4). The NP shape is also different, as can be observed in the insets of Fig. 1(a) and (b): faceted NPs, with an irregular profile are visible on the tips of the ZnSe NWs grown with an excess of Se, while spherical NPs are found on the tips of the NWs grown under Zn-rich conditions. The differences in the morphology of the NWs and the shape of the NPs suggest that two distinct growth modes take place under the two opposite Zn/Se pressure ratios, even if the NW length, *i.e.* the growth rate, is comparable.

Let us now focus our attention on the NPs assisting the growth, and on their interaction with Zn and Se fluxes. In Fig. 2 we show how XPS and XRD measurements of the Au covered GaAs(111)B substrate are affected by the thermal annealing. In Fig. 2(a) we show the XPS spectra of the Au 4f core level measured *in situ* at RT and after 10 minutes annealing at different temperatures. The 4f_{7/2} peak has the same shape and position (binding energy BE = 84.00 eV, spin-orbit splitting Δ_{SO} = 3.68 eV) after RT deposition and after annealing at 300 °C, tracing the signal of pure metallic Au.²⁷ Conversely, from 400 °C upwards, a progressive shift in the peak position toward higher binding energies is observed. This indicates the occurrence of a chemical interaction between the gold film and the substrate, *i.e.* the interdiffusion of Ga atoms from the substrate into the Au layer and the formation of a Au–Ga alloy phase, followed by As desorption.²⁸ The difference in the peak position with respect to that of pure gold reflects the amount of Ga in the alloy, which is greater for higher temperatures.^{28,29} In particular, after

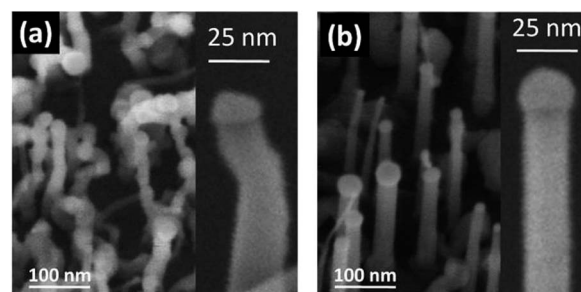


Fig. 1 Tilted-view SEM images of ZnSe NWs obtained after 10 minutes deposition at 450 °C with a BPR of 0.4 (Se-rich) (a) and 4 (Zn-rich) (b). The insets are magnified images of representative nanowires shown in the corresponding panels.

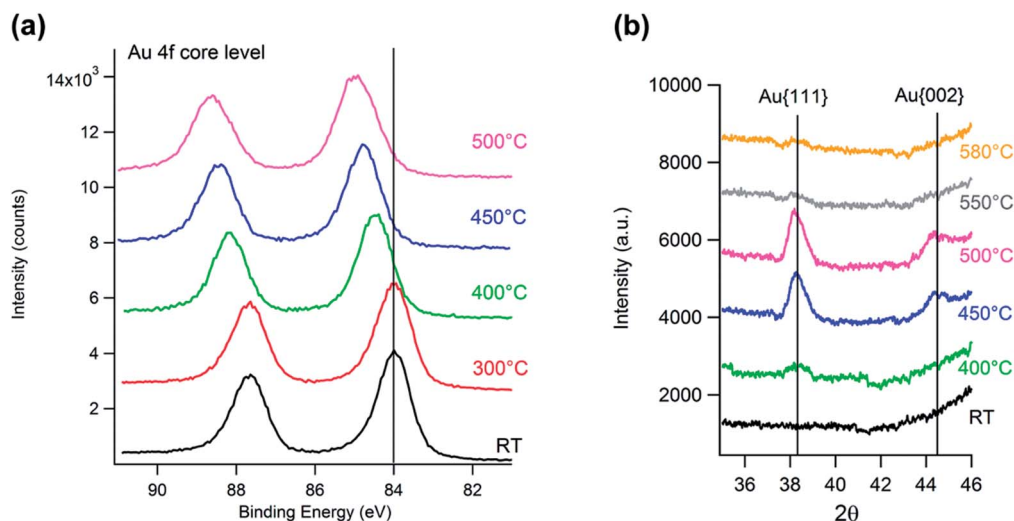


Fig. 2 (a) XPS spectra of the Au 4f core level of the metal film deposited on GaAs(111)B at room temperature and after annealing at the different temperatures. The line at 84.00 eV indicates the position of the 4f_{7/2} peak of pure Au. A clear blue-shift of the binding energy of the 4f core level electrons is observed, which indicates an increasing interaction of the Au metal film with the GaAs substrate. (b) Grazing incidence XRD patterns of the nanoparticles as a function of temperature. The Au diffraction peaks are detected up to 550 °C, when they disappear, suggesting the melting of the NPs.

annealing at 450 °C, the Au 4f_{7/2} peak has a binding energy of 84.65 eV. This core-level binding energy could be ascribed to an alloy with a Ga atomic fraction of 0.33 or slightly less if nanometer-sized clusters are measured instead of bulk alloys.²⁸ Based on the Au–Ga binary system,³⁰ Au–Ga alloys with a Ga mole fraction in the range between 0.22 and 0.45 are in the molten state at 450 °C. This suggests the presence of a liquid Au–Ga alloy instead of solid Au at the surface of the nanoparticles. However, the limited escape depth of the XPS technique ($\lambda = 1.5$ nm in our setup) prevents us from discriminating between the formation of nanoparticles with a homogeneous composition and limited surface alloying. In order to verify the physical state and the phase transition of the Au nanoparticles due to alloying with Ga during annealing, Au-covered samples were analyzed by grazing incidence XRD as a function of the annealing temperature. In Fig. 2(b) we show the XRD powder spectra at different temperatures, within the 2θ range in which the most intense signals of Au are expected. We did not get any powder diffraction patterns at low temperatures because of the epitaxial nature of the metal film deposited on deoxidized GaAs(111)B.³¹ The dewetting process begins to be effective at 400 °C when weak Au diffraction peaks appear. The intensity of the diffraction peaks increases at 450 °C and the signals are detectable up to 550 °C, when they disappear, suggesting the melting of the nanoparticles.

The diffraction peaks are quite broad, because of the nanometer-sized diameter of the nanoparticles. Due to this broadening, and the close similarity between the lattice constant of gold and of gold-rich solid Au–Ga solutions,^{31,32} the distinction between these two phases has not been possible. However, a solid phase is clearly present up to 550 °C. Such a phase could be either pure gold or a gold–gallium solid solution with a Ga molar fraction smaller than 0.22.³⁰

Combining the results of the XPS and XRD analysis, we can speculate that the metal NPs obtained by dewetting the Au film on GaAs(111)B at 450 °C have a liquid Au–Ga alloy shell, and a solid core made of pure Au or a Au-rich solid solution. This picture is supported by a theoretical study by Kratzer *et al.*³³ about the energetics of As, Ga and Au(111) as a model system for gold NPs involved in the growth of GaAs NWs. They demonstrated that the coexistence of a Ga–Au surface solution and an ordered phase of Au₇Ga₂ in the catalyst particle is likely, since the formation of Ga substitution in the topmost layers is more favorable than in the subsurface Au layers. Although they considered Ga atoms impinging from the gas phase, the tendency to form a surface alloy due to the lower diffusion barrier and the lower formation energy for the Au–Ga alloy at the NP surface can also be supposed in the case of Ga atoms coming from the substrate.

It is worth noting that the size distribution of the NPs is quite broad, thus their composition and physical state at the same temperature could not be the same for all of them. For instance, smaller NPs could have a homogeneous composition and be completely liquid at 450 °C, whereas bigger ones could have an inhomogeneous phase, with the Ga concentration decreasing from the surface to the center. Tchernycheva *et al.*⁸ showed *in situ* reflection high energy electron diffraction (RHEED) and TEM evidence of Au NP phase transition during the annealing of a thin gold film on GaAs(111)B. They reported the range between 340 and 400 °C as the phase transition temperature window in which the complete melting of Au–Ga alloy NPs with diameters from 5 to 15 nm is observed. Moreover, they found a size-dependent composition of the re-crystallized particles under As-flux, suggesting that the amount of Ga in the NPs, *i.e.* their composition, depends both on the substrate temperature and particle size. We also believe that in our case, the composition of the NPs obtained at 450 °C could be size-sensitive, thus

some of them could be liquid (most probably the smallest) and some others could have a liquid shell and a Au-rich solid core.

The impact of Se and Zn beams on the chemical composition of the Au–Ga alloy NPs was revealed by the analysis of the NP morphology and the Au 4f core-level emission after exposing the annealed samples to the individual fluxes. Fig. 3 shows the SEM images of the NPs after dewetting (a) and after exposing the annealed samples at Zn (b) or Se (c) fluxes for 1 minute at 450 °C. Fig. 3(d) displays the corresponding Au 4f core-level spectra.

The Zn beam does not alter the chemical composition of the Au–Ga NPs, as suggested by the Au 4f peak position, which is the same before and after the Zn exposure (Au 4f_{7/2} BE = 84.65 eV). The morphology of the resulting NPs (Fig. 3(b)) is also very similar to that of the NPs shown in Fig. 3(a), which were obtained by annealing the Au-covered sample at 450 °C without any Zn or Se beams. Conversely, the Au 4f peak of the NPs exposed to the Se beam is back-shifted to a binding energy of 84.00 eV, which is the peak position of metallic gold. The SEM image of such NPs (Fig. 3(c)) shows some relevant differences:

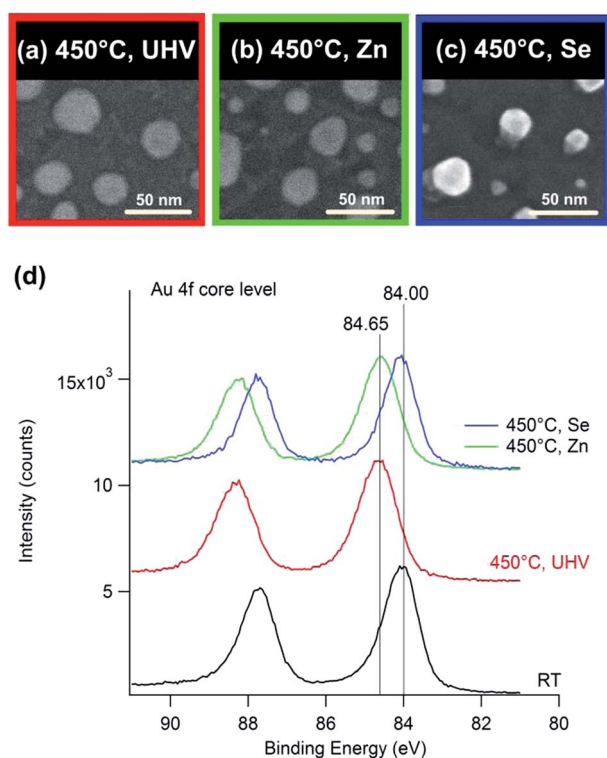


Fig. 3 Morphology and XPS spectra of the Au NPs after their interaction with the GaAs substrate and Zn or Se fluxes at 450 °C. (a–c): SEM images of the Au NPs annealed in an ultra-high vacuum (red frame), after the interaction with the Zn flux (green frame) and after the interaction with the Se flux (blue frame). The same color code is used in the XPS spectra in the lower panel (d): the red curve indicates an increase of the binding energy of the Au 4f electrons when the temperature (450 °C) allows the Au film to interact with the substrate (compared with the black curve taken at room temperature); no further change is observed when the annealed NPs interact with the Zn flux (green curve), while the original binding energy is recovered when the annealed NPs interact with the Se flux (blue curve).

the particles are more faceted, and a step underneath them is clearly visible. Furthermore, they have a different image contrast, suggesting a different electrical and chemical composition.

These results suggest that the Se beam reacts with the Ga atoms of the Au–Ga alloy NPs, giving a Ga_xSe_y solid compound that precipitates and leaves behind pure Au nanocrystals.

When the ZnSe nanowires grow, Zn and Se beams are simultaneously supplied on the Au–Ga alloy NPs. After 1 minute of ZnSe deposition at a BPR of 4, the Au 4f_{7/2} peak is still centered at 84.65 eV, whereas after the same deposition time at a BPR of 0.4, it is back-shifted toward the pure gold position (ESI†). The picture that emerges from the data is shown in Fig. 4(a) which describes the core of our work: under Zn-rich conditions (BPR = 4), the supplied Se mainly reacts with Zn atoms to give the ZnSe crystal, and the one-dimensional growth is promoted by liquid Au–Ga alloy NPs, or solid Au-rich particles surrounded by a liquid Ga-rich shell (VLS mode). On the other hand, when the Au–Ga alloy NPs are exposed to Se-rich vapors (BPR = 0.4), the excess Se reacts with Ga atoms, depleting the alloy particles and making them solidify at the very beginning of the deposition. The NW growth now proceeds, assisted by Au solid nanocrystals (VSS mode). Indeed the Au–Zn³⁴ and the Au–Se³⁵ binary systems show only high-temperature melting compounds, and even if the melting point could be lowered due to size-effects,³⁶ this would not play a significant role in our case, since the difference between the lowest eutectic temperature (659 °C) and the NW growth temperature (450 °C) is too large. We thus believe that as soon as the Se beam reacts with Ga atoms of the Au–Ga alloy droplets, the NPs become solid and remain solid during the growth of the NWs. Au assisted vapor–solid–solid growth of the ZnSe NWs on the ZnSe substrate at temperatures as high as 500 °C has indeed been recently reported.¹⁸

The different wire morphologies obtained with the two opposite BPRs, result from the two different growth mechanisms, as schematically illustrated in Fig. 4(a). It is widely known that growth from solid seed particles often suffers from the problem of a less controlled growth direction.^{4,37} Solid particles are less uniform in shape and may have varying facets, producing nanowires with less uniform shapes. On the contrary, liquid NPs, or a liquid shell around the NPs, may provide a more uniform and isotropic medium for NW nucleation and growth. Moreover, the diffusivity through a liquid particle is usually faster than that through a solid particle, hence the probability for the impinging atoms to find a nucleation site before reaching the nanoparticle–nanowire interface, leading to a change in the growth direction, is higher for solid NPs. This indeed results in the growth of kinked NWs, as observed when ZnSe NWs are grown under Se-rich conditions. On the other hand, the liquid state of the surface layers alone may not be sufficiently efficient to give a measurably faster growth rate.

High-resolution TEM images of the NW tips are shown in Fig. 4(b) and (c). The lattice structure and parameter of the faceted NP of Fig. 4(b), on the tip of a worm-like ZnSe NW grown in excess Se, is consistent with that of a Au fcc crystal. A significant amount of particles containing two crystal grains are

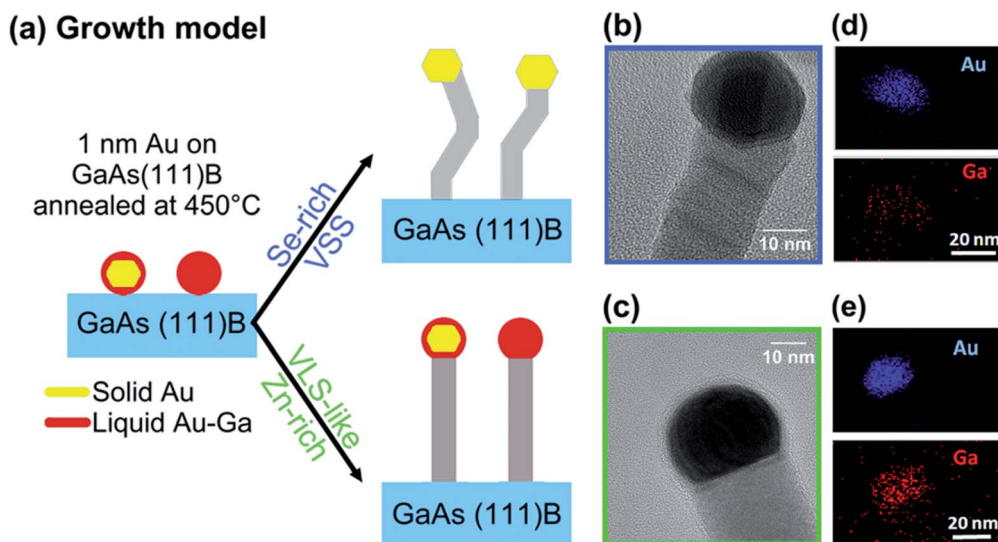


Fig. 4 (a) A schematic view of the BPR-dependent ZnSe NW growth mechanisms. The thermal dewetting of the Au film on GaAs(111)B leads the formation of Au–Ga alloy nanoparticles that could be either totally liquid, or solid with a liquid shell. Using Se-rich conditions, the excess Se reacts with the alloy nanoparticles, draining out Ga atoms and making them solidify. The NW growth goes on, assisted by solid Au nanocrystals (VSS mode), leading to the formation of kinked ZnSe NWs. On the other hand, in Zn-rich conditions, all the Se supplied reacts with the Zn beam. Therefore the growth is assisted by Au–Ga alloy NPs in the VLS-like mode, which leads to the growth of straight and uniformly oriented NWs. (b and c) HRTEM images and (d and e) EDX elemental maps of the NPs on the tips of two ZnSe NWs grown under Se-rich (b and d) and Zn-rich (c and e) conditions.

found on the tips of these wires, both having the lattice parameter of fcc Au (ESI†). The presence of the two grains may be due to the coexistence of two phases at 450 °C (the Au solid core and the Au–Ga liquid alloy shell) and the subsequent fast solidification of the liquid phase due to the Ga removal. On the other hand, most of the spherical shaped NPs found on the tips of the NWs grown in Zn-rich conditions (Fig. 4(c)) have a lattice that is not compatible with a pure Au phase, but rather close to the Au_7Ga_2 hexagonal compound.

STEM-EDX analysis of several ZnSe NWs reveals the presence of 7–15% Ga, averaged on the NP volume, on the tips of the NWs grown in Zn-rich conditions (Fig. 4(e)). In the NPs of the wires grown in Se-rich conditions (Fig. 4(d)) this value drops below 5%, close to our detection limit.

The NW body consists of stoichiometric ZnSe for both kinds of wire. NWs grown under Zn-rich conditions have a wurtzite crystal structure with the c axes parallel to the growth direction for the whole length, whereas wires grown at a BPR of 0.4 also have a wurtzite crystal structure, but with a higher density of stacking faults and an ill-defined growth direction. Moreover, their interface with the NP is rarely flat and perpendicular to the growth direction.

Nanowire growth through different growth mechanisms at the same temperature has already been reported for other systems. For instance, Heun *et al.*³⁸ suggest the coexistence of VLS and VSS growth in Pd-assisted InAs NWs grown by chemical beam epitaxy; Kodambaka *et al.*¹⁰ also reported the presence of both solid and liquid seed particles during Ge NW growth, observed by *in situ* TEM. Hillerich *et al.*¹¹ showed the simultaneous growth of two types of InP NWs side by side on the same substrate, assisted by solid Cu_2In and liquid In-rich

particles. In all these systems, the NP properties (diameter, thermal history and chemical composition) make a difference. The occurrence of either mechanism, depending on the NP composition is a very attractive issue that suggests the possibility to select the wire's properties through the control of the dynamic process happening inside or at the surface of the nanoparticle. For the system studied in this work, the Se-induced changes in the NP composition allow us to choose the growth mechanism and, in this case, change the morphology of the NWs during their growth. Fig. 5 shows ZnSe NWs grown for 15 minutes in Zn-rich conditions and, after a rapid BPR switch, a further 15 minutes growth in excess Se. Similar results are also obtained if the growth occurs under Zn-rich conditions for the whole time, but a 1 minute-long interruption of the Zn flux is provided at any moment during the growth (not shown). In both cases, as soon as the Au–Ga alloy NPs undergo an excess of Se, with the ensuing reaction of Ga with Se and the sudden solidification of the nanoparticle, the wire kinks. Afterwards the growth goes on, led by a solid Au particle, towards the formation of a worm-like upper part of the NW. An excess of Ga can be detected by EDX at the BPR switch point, suggesting the effectiveness of such a mechanism (Fig. 5(d) and (e)).

On the other hand, if we maintain Zn-rich conditions for the whole deposition time, the growth of uniformly straight and long ZnSe NWs is achieved (see Fig. 6(a)), with spherical Au–Ga NPs on their tips. If these NWs are then exposed to a Se flux for only a few minutes at the end of the growth, the NPs on their tips change shape and composition (see Fig. 6(b)), becoming pure Au faceted nanocrystals. The depletion from Ga of Au–Ga nanoparticles following after-growth exposure to

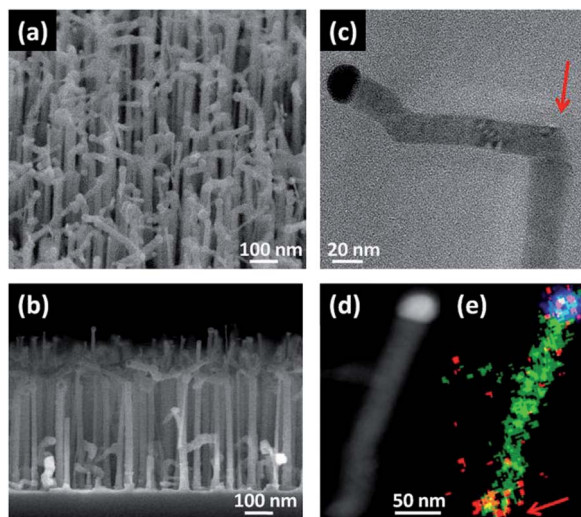


Fig. 5 (a and b) Tilted-view and cross-view SEM images of ZnSe NWs grown for 15 minutes at a BPR of 4 followed by 15 minutes at a BPR of 0.4. (c) A TEM image of a nanowire in which the two portions grown under opposite conditions are clearly visible. (d and e) STEM and EDX map of a NW broken at the BPR switch point, *i.e.* at the kink. Color index: Zn K: light green; Se K: dark green; Au M: blue; Ga K: red. The red arrows indicate the BPR switch point.

As was already observed in the case of GaAs NWs.^{39,40} The purification of the NP was accompanied by the formation of a GaAs “neck” due to the reaction of Ga atoms from the

nanoparticle with the As beam. Interestingly in our case, such “Se-purified” NPs show a diameter-dependent crystal structure: small particles are regular multiply twinned icosahedral nanoparticles (MTPs), while large NPs are fcc crystals still containing twin boundaries (Fig. 6(c) and (d)). It is known that MTPs are regular structures that form upon rapid quenching from the liquid state and are stable up to a diameter of about 15 nm.^{41–43} As the size of a cluster increases, these structures become less favorable due to accumulated strain energy. Therefore bigger nanoparticles crystallize into the more stable fcc structure with some residual twins. The presence of icosahedral gold particles at the tips of these nanowires indirectly confirms that the seed NPs were in the liquid state during the growth, becoming solid as the Se beam alone is supplied, due to the fast depletion from the Ga atoms. Moreover, a “neck” between the particle tip and the NW body is obtained after this treatment (Fig. 6(d)). This “neck” is mainly crystalline but with variable spacing and orientation, and the EDX map shows an accumulation of gallium therein (Fig. 6(e)). We cannot exclude that a slow release of Ga from the NP to the NW body may also take place during growth in Zn-rich conditions, giving a distribution of Ga impurities in the NW body below the detection limit of EDX measurements. As a matter of fact, the extremely good alignment of NWs observed in Fig. 6(a) gets progressively worse in the case of growth longer than 1.5 μm (not shown), suggesting a progressive depletion of the NP and solidification of the shell.

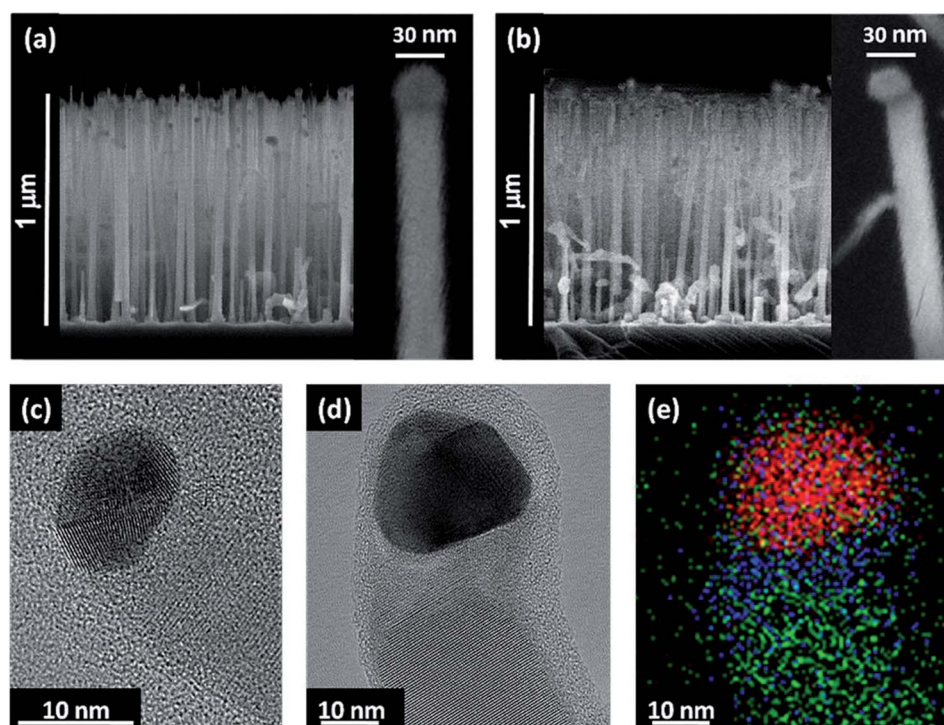


Fig. 6 (a) ZnSe nanowires grown at a BPR of 4 (Zn-rich) for 30 minutes. (b) The same wires kept for 1 minute under a Se flux at the end of the growth. The insets on the right are magnified SEM images of transferred nanowires, in which the different nanoparticle shapes are clearly visible. (c and d) HRTEM images of two NWs of the sample shown in panel (b), with different diameters and NP crystal structures: multiply twinned icosahedral nanoparticles (MTP) (c) and fcc (d). (e) EDX map of the wire shown in (d). Au M: red, Ga K: blue, Zn K: green.

Conclusions

In this work we have shown that, given the necessary thermal budget, an interplay between seed–substrate interaction and elemental flux supply occurs. Based on this, we can tune the NW growth mechanism from being VLS-based to become VSS-like. In particular, we have shown that the thermal diffusion of Ga atoms from the substrate into the Au seed NPs leads to the formation of a liquid Au–Ga alloy at the NP surface. The chemical composition and physical state of such NPs are strongly affected by the Se flux. Therefore, using Zn-rich conditions, the growth of ZnSe NWs occurs through the VLS growth mode, assisted by Au–Ga alloy droplets that could be either completely liquid, or solid with a liquid shell. On the other hand, if Se-rich conditions are used, the NW growth mechanism is switched toward the VSS mode, assisted by solid Au nanocrystals. The growth mechanism has a profound impact on the NW morphology and crystal quality. Indeed, at a high Zn/Se ratio, straight and uniformly oriented ZnSe NWs are obtained, whereas at low a Zn/Se ratio, kinked and worm-like NWs grow. In the former case, the crystal structure of the NW is of a higher quality with a strongly reduced density of defects, with the wurtzite phase dominating in the NWs in both cases. These results constitute an interesting example of how alloyed foreign metal particles, in this case Au–Ga NPs obtained by annealing of Au on GaAs, and preserved by growth under Zn-rich conditions, may be optimal for the growth of semiconductor NWs, as recently suggested by Dick *et al.*⁴⁴ We have shown that the switch from one growth mechanism to the other is possible within a single growth and that this change has immediate effects on the wire's morphology. Furthermore, we have demonstrated that different growth terminations affect the chemical composition and crystal structure of the nanoparticles on the nanowire tips.

The conclusions of this work have been deduced by experiments on ZnSe NWs, but we are convinced that they are valid in all systems where the interaction of the seed with the substrate and the beam fluxes induces changes in the physical state of the NPs.

Experimental

ZnSe nanowires were grown by solid source molecular beam epitaxy (MBE) in a multi-chamber ultra-high-vacuum facility. The GaAs(111)B substrates were first deoxidized at 600 °C in the III–V chamber. A 1 nm thick Au layer was deposited at room temperature in the metallization chamber and then the samples were transferred into the II–VI growth chamber, where 10 minutes annealing at 450 °C was followed by ZnSe deposition at the same temperature. We used elemental Zn and Se sources, fluxes corresponding to a two-dimensional ZnSe growth rate of 0.5 $\mu\text{m h}^{-1}$ at 280 °C, and a Zn-to-Se beam pressure ratio (BPR) of 0.4 (Se-rich conditions) and 4 (Zn-rich conditions). The Au film dewetting process during the annealing was studied by *in situ* X-ray photoemission spectroscopy (XPS) and *ex situ* grazing incidence X-ray diffraction (XRD). The XPS analysis was carried out before and after the annealing in the Al-K α photoemission chamber connected to the MBE system, whereas the powder

XRD patterns were collected as a function of the annealing temperature at the MCX beamline of an Elettra synchrotron radiation source, operating at 8 keV and equipped with a furnace end-station.⁴⁵ The morphology of the ZnSe nanowires was characterized using a Zeiss SUPRA40 Scanning Electron Microscope. Transmission Electron Microscopy (TEM) was performed using a JEOL 2200 microscope operated at 200 keV and with a Scherzer resolution in TEM and Scanning TEM (STEM) of 0.19 nm and 0.14 nm respectively. The microscope was equipped with EDX and Ω -filter for energy loss analyses.

Notes and references

- 1 R. Agarwal and C. M. Lieber, *Appl. Phys. A: Mater. Sci. Process.*, 2006, **85**, 209–215.
- 2 R. Yan, D. Gargas and P. Yang, *Nat. Photonics*, 2009, **3**, 569–576.
- 3 P. Yang, R. Yan and M. Fardy, *Nano Lett.*, 2010, **10**, 1529–1536.
- 4 M. E. Messing, K. Hillerich, J. Johansson, K. Deppert and K. A. Dick, *Gold Bull.*, 2009, **42**, 172–181.
- 5 M. C. Plante, J. Garrett, S. C. Ghosh, P. Kruse, H. Schriemer, T. Hall and R. R. LaPierre, *Appl. Surf. Sci.*, 2006, **253**, 2348–2354.
- 6 A. Rath, J. K. Dash, R. R. Juluri, A. Rosenauer, M. Schoewalter and P. V. Satyam, *J. Appl. Phys.*, 2012, **111**, 064322.
- 7 M. E. Messing, K. Hillerich, J. Bolinsson, K. Storm, J. Johansson, K. A. Dick and K. Deppert, *Nano Res.*, 2010, **3**, 506–519.
- 8 M. Tchernycheva, J. C. Harmand, G. Patriarche, L. Travers and G. E. Cirlin, *Nanotechnology*, 2006, **17**, 4025–4030.
- 9 S. C. Ghosh, P. Kruse and R. R. LaPierre, *Nanotechnology*, 2009, **20**, 115602.
- 10 S. Kodambaka, J. Tersoff, M. C. Reuter and F. M. Ross, *Science*, 2007, **316**, 729–732.
- 11 K. Hillerich, K. A. Dick, M. E. Messing, K. Deppert and J. Johansson, *Nano Res.*, 2012, **5**, 297–306.
- 12 A. D. Gamalski, J. Tersoff, R. Sharma, C. Ducati and S. Hofmann, *Nano Lett.*, 2010, **10**, 2972–2976.
- 13 A. D. Gamalski, J. Tersoff, R. Sharma, C. Ducati and S. Hofmann, *Phys. Rev. Lett.*, 2012, **108**, 255702.
- 14 P. Madras, E. Dailey and J. Drucker, *Nano Lett.*, 2009, **9**, 3826–3830.
- 15 M. Kolibal, T. Vystavel, P. Varga and T. Sikola, *Nano Lett.*, 2014, **14**, 1756.
- 16 P. Caroff, K. A. Dick, J. Johansson, M. E. Messing, K. Deppert and L. Samuelson, *Nat. Nanotechnol.*, 2009, **4**, 50–55.
- 17 B. Tian, P. Xie, T. J. Kempa, D. C. Bell and C. M. Lieber, *Nat. Nanotechnol.*, 2009, **4**, 824–829.
- 18 E. Bellet-Amalric, M. Elouneq-Jamroz, P. Rueda-Fonseca, S. Bounouar, M. Den Hertog, C. Bougerol, R. André, Y. Genuist, J. P. Poizat, K. Kheng, J. Cibert and S. Tatarenko, *J. Cryst. Growth*, 2013, **378**, 233–237.
- 19 A. Colli, S. Hofmann, A. C. Ferrari, C. Ducati, F. Martelli, S. Rubini, S. Cabrini, A. Franciosi and J. Robertson, *Appl. Phys. Lett.*, 2005, **86**, 153103.

- 20 J. Basu, R. Divakar, J. Nowak, S. Hofmann, A. Colli, A. Franciosi and C. B. Carter, *J. Appl. Phys.*, 2008, **104**, 064302.
- 21 V. Zannier, F. Martelli, V. Grillo, J. R. Plaisier, A. Lausi and S. Rubini, *Phys. Status Solidi RRL*, 2014, **8**, 182–186.
- 22 Y. Cai, S. K. Chan, I. K. Sou, Y. F. Chan, D. S. Su and N. Wang, *Adv. Mater.*, 2006, **18**, 109–114.
- 23 Y. Liang, Y. Tao and S. K. Hark, *CrystEngComm*, 2011, **13**, 5751.
- 24 K. B. Kahan, I. A. Goldthorpe and J. Minter, *J. Cryst. Growth*, 2011, **322**, 57–62.
- 25 C. Fernandes, H. Ruda, A. Saxena and C. De Souza, *Phys. Status Solidi C*, 2012, **9**, 2460–2464.
- 26 K. Imai, K. Kumazaki, T. Haga and Y. Abe, *J. Cryst. Growth*, 1988, **91**, 617–622.
- 27 P. Citrin, G. Wertheim and Y. Baer, *Phys. Rev. Lett.*, 1978, **41**, 1425–1428.
- 28 G. Petro, T. Kendelewicz, I. Lindau and W. E. Spicer, *Phys. Rev. B: Condens. Matter Mater. Phys.*, 1986, **34**, 7089–7106.
- 29 J. A. Nicholson, J. D. Riley, R. C. G. Leckey, J. G. Jenkin, J. Liesegang and J. Azoulay, *Phys. Rev. B: Condens. Matter Mater. Phys.*, 1978, **18**, 2561–2567.
- 30 J. Liu, C. Guo, C. Li and Z. Du, *J. Alloys Compd.*, 2010, **508**, 62–70.
- 31 S. Leung and A. G. Milnes, *Thin Solid Films*, 1983, **104**, 109–131.
- 32 D. D. L. Chung and E. Beam III, *Thin Solid Films*, 1985, **128**, 299–319.
- 33 P. Kratzer, S. Sakong and V. Pankoke, *Nano Lett.*, 2012, **12**, 943–948.
- 34 H. S. Liu, K. Ishida, Z. P. Jin and Y. Du, *Intermetallics*, 2003, **11**, 987–994.
- 35 T. B. Massalski, *Binary Alloy Phase Diagrams*, ASM International, Materials Park, Ohio, 2nd edn, 1990, vol. 1.
- 36 P. Buffat and J.-P. Borel, *Phys. Rev. A*, 1976, **13**, 2287–2298.
- 37 S. V. Thombare, A. F. Marshall and P. C. McIntyre, *J. Appl. Phys.*, 2012, **112**, 054325.
- 38 S. Heun, B. Radha, D. Ercolani, G. U. Kulkarni, F. Rossi, V. Grillo, G. Salviati, F. Beltram and L. Sorba, *Small*, 2010, **6**, 1935–1941.
- 39 J. C. Harmand, G. Patriarche, N. Péré-Laperne, M.-N. Mérat-Combes, L. Travers and F. Glas, *Appl. Phys. Lett.*, 2005, **87**, 203101.
- 40 A. I. Persson, M. W. Larsson, S. Stenström, B. J. Ohlsson, L. Samuelson and L. R. Wallenberg, *Nat. Mater.*, 2004, **3**, 677–681.
- 41 Y. G. Chushak and L. S. Bartell, *J. Phys. Chem. B*, 2001, **105**, 11605–11614.
- 42 G. Rossi and R. Ferrando, *Nanotechnology*, 2007, **18**, 5706.
- 43 S. D'Addato, V. Grillo, S. Altieri, R. Tondi, S. Valeri and S. Frabboni, *J. Phys.: Condens. Matter*, 2011, **23**, 175003.
- 44 K. A. Dick and P. Caroff, *Nanoscale*, 2014, **6**, 3006–3021.
- 45 P. Riello, A. Lausi, J. Macleod, J. R. Plaisier, G. Zeraushek and P. Fornasiero, *J. Synchrotron Radiat.*, 2013, **20**, 194–196.